scientific reports

Check for updates

OPEN

Influence of wave impedance of backfill medium on explosive stress wave propagation and rock mass damage evolution

Hanqiu Wang✉, Chengyong Liu, Xinfu Zhang & Hengjian Qiu

In engineering practices such as backfill mining, the existence and characteristics of the rock-backfill interface significantly influence the propagation of explosive stress waves and the dynamic response of the rock mass. This study aims to reveal how, among these characteristics, different backfill media and their wave impedance differences with the rock specifically affect these processes. To this end, physical experiments were combined with numerical simulations, utilizing Digital Image Correlation (DIC) technology to capture strain field evolution under blasting, and LS-DYNA was employed for numerical analysis. The research indicates that the wave impedance difference between the rock and the backfill medium is key to controlling stress wave propagation and energy distribution. When the wave impedances are similar, stress wave transmission is dominant, leading to higher peak strain values at various points and a more uniform action of the stress wave on the rock mass, resulting in relatively uniform final failure. When the wave impedance difference is large, interface reflection is enhanced, forming a significant "blocking effect"; in this case, although the initial peak strain may be lower, the continuous action of the interface can lead to greater final strain and plastic deformation in the rock mass. Numerical simulations further show that the greater the wave impedance difference, the more pronounced the "guiding" and "blocking" effects of the backfill on crack propagation. This leads to intensified damage and crack accumulation in the rock mass adjacent to the backfill due to energy concentration, which also results in a higher fractal dimension of the cracks. Therefore, the type of backfill medium directly determines the strain response characteristics and final damage patterns of the rock mass by modulating the reflection and transmission behavior of waves at the interface. These findings have practical guiding significance for optimizing backfill material selection and blasting parameter design in backfill mining.

Keywords Blasting, Backfill, Explosive stress wave, Wave impedance, Rock-backfill interface

As a typical heterogeneous geological material, rock mass universally contains structural discontinuities such as filled defects, voids, and joints[1–3]. In mining engineering employing the drilling and blasting method, the interaction of high-energy stress waves generated by explosive detonation with these discontinuities can significantly alter wave propagation characteristics, thereby affecting rock fragmentation efficiency and potentially inducing engineering instability[4–6]. Existing research indicates that the modulating effect of such discontinuities on stress wave propagation is one of the key factors inducing dynamic hazards in underground engineering; therefore, an in-depth investigation into the propagation mechanism of explosive stress waves in rock masses containing discontinuities holds significant importance for engineering safety[7].

To understand how rock mass discontinuities influence explosive stress wave propagation and fracturing, researchers have systematically applied a combination of theoretical analysis, experimental verification, and numerical modeling. At the theoretical level, Ma et al.[8] evaluated the equivalent medium method for jointed rock masses and further refined their proposed equivalent viscoelastic medium model, analyzing the advantages, disadvantages, and applicability of different equivalent methods to discontinuous rock masses. Zhao et al.[9] investigated the transmission characteristics of elastic P-waves normally incident on a single dry crack, considering the nonlinear normal deformation of the crack. They compared the differences between linear and nonlinear models and found that the transmission and reflection coefficients of the linear model

China Coal Energy Research Institute Co., Ltd, Xi'an 710054, Shaanxi, People's Republic of China. ✉email: whq32001@vip.qq.com

are special cases of the nonlinear model. Li et al.[10,11] noted the asymmetry in the closing and opening behavior of rock joints and, for the first time, derived a wave propagation equation for joints with asymmetric closing-opening characteristics, expressing it in a time-differential form. Furthermore, Dong et al.[12,13] incorporated two additional phenomena into their analysis: first, the influence of in-situ stress on both physical and geometrical attenuation of cylindrical waves, and second, the effects of wave-joint interactions. This comprehensive approach culminated in the formulation of a new propagation equation for cylindrical waves within stressed, jointed rock masses.

Experimentally, based on wave propagation experiments using artificial rock joints, Chen et al.[14] established that the transmission coefficient is governed by the joint's contact state, identifying both the contact area ratio and joint thickness as critical influencing factors. Han et al.[15] examined how stress waves propagate and dissipate energy when passing through rock joints filled with cement mortar. The study's findings reveal that joint thickness is inversely related to several key parameters. Specifically, as the joint thickens, the transmission coefficient, dynamic strength, and energy absorption rate all diminish. In contrast, the reflection coefficient, peak strain, and degree of joint closure exhibit a corresponding increase; moreover, the deformation of the cement mortar joint was the primary cause of the overall deformation and failure of the specimen. Jia et al.[16] systematically investigated how the loading rate influences the mechanical and wave-transmission properties of rock joints. Their analysis specifically correlated the loading rate with resulting changes in stress-closure curves, joint specific stiffness, and transmission coefficients. Huang et al.[17] investigated how water content affects stress wave propagation in filled viscoelastic joints. They found that an increase in water content enhances the joint's viscosity (characterized by the quality factor), thereby increasing the equivalent stiffness and promoting energy dissipation, which produces a dual effect on stress wave propagation. Wang et al.[18] found that increasing the angle between a blast hole and a rock joint decreases effective stress in rock, as the joint's influence on wave reflection and superposition weakens, leading to lower peak effective stress. Zhang et al.[19], using a digital laser dynamic caustics experimental system, analyzed the "guiding" and "blocking" effects of the filling medium, emphasizing the role of the infill's ductility on the damage degree of the blasted medium. Furthermore, some studies have also explored the influence of defect shape, size on the mechanical properties of rocks[20–24].

Given the random nature and operational challenges of blasting experiments, numerical simulation has emerged as a crucial research tool[25]. Using the Discrete Element Method (DEM), Zhu et al.[26] established a critical threshold for when joints dominate wave behavior: this occurs when the wave's tensile stress amplitude exceeds the joint's tensile strength. Their parametric study further quantified the influence of depth and various joint properties (stiffness, spacing, inclination, and intersection angle) on wave propagation and cavern stability. Adopting a different approach, Yu et al.[27] employed micromechanical damage mechanics to simulate failure processes. Their model successfully replicated acoustic emission characteristics and underscored that the ultimate damage patterns are governed by the transmitted wave energy and the width of the joints.

The aforementioned studies, through theoretical, experimental, and simulation methods, have progressively revealed the impact of filled defects on explosive stress wave propagation, considering aspects from geometric parameters (such as thickness, inclination, shape), mechanical properties and the dynamic response. However, current research still has limitations: the filling media studied are often confined to single materials, whereas in natural rock masses, filling media frequently exhibit high complexity. The influence of different types of filling media on the wave propagation characteristics is a complex and critical research area that urgently requires further exploration of their specific interaction mechanisms.

Addressing the aforementioned research status and deficiencies, this paper focuses on the dominant role of wave impedance differences at the rock-backfill interface on explosive stress wave propagation, energy partitioning, and the dynamic damage and fracture behavior of the rock mass. By employing backfill materials with different wave impedances to simulate varying degrees of wave impedance difference, and combining high-speed photography with Digital Image Correlation (DIC) synchronous measurement technology, model blasting experiments were conducted and numerical simulations were performed. This aims to analyze the full-field strain evolution under blasting load, the complex effects of interface waves, and the crack propagation patterns in the rock mass. This research is dedicated to deepening the understanding of the dynamic response and damage mechanisms of rock masses containing backfill interfaces under different wave impedance conditions, thereby providing scientific support for blasting design optimization, backfill material selection, and surrounding rock stability assessment in backfill mining engineering.

Description of mechanical processes

Interaction of stress waves with backfill

Figure 1 provides a schematic diagram illustrating the interaction between an explosive stress wave and the rock-backfill interface. When the stress wave encounters the rock-backfill interface, the explosion stress can be decomposed into: shear stress along the rock-backfill interface (σ_{xy}) and normal stress perpendicular to the interface (σ_{yy}). The relationship between them is shown in Eq. (1):

$$\begin{aligned} \sigma_{yy} &= \sigma_{xx} \cos \alpha \\ \sigma_{xy} &= \sigma_{xx} \sin \alpha \end{aligned} \tag{1}$$

In the equation, σ_{xx} is the explosion stress of the incident wave, and α is the angle between the incident wave and the rock-backfill interface. Under the action of normal stress, the backfill is subjected to compression, and under the action of shear stress, the backfill and the rock will experience relative slip along the interface.

Due to chemical cementation, there is a certain bond strength between the backfill and the rock interface. The shear strength at the interface (τ_{xy}) is determined by cohesion (c) and the internal friction angle (φ):

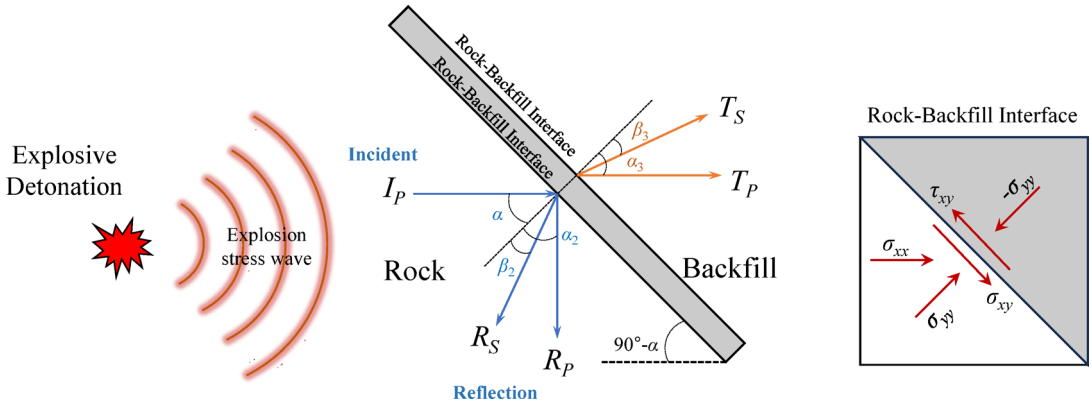

Fig. 1. Interaction of stress wave with backfill.

$$\tau_{xy} = \sigma_{yy} \tan \varphi + c \tag{2}$$

Therefore, the stress equilibrium conditions at the rock-backfill interface are as follows:

$$\sigma_f = \sigma_{xy} - \tau_{xy} = \sigma_{xx} \sin \alpha - \sigma_{xx} \cos \alpha \tan \varphi - c \tag{3}$$

When σ_f is greater than 0, relative sliding will occur between the rock and the backfill along the interface. The critical condition for slip initiation depends on the comparison between the shear stress and the interface strength.

Wave mode conversion and reflection/transmission coefficients

The wave impedance mismatch between the rock and backfill materials is the primary driver for wave mode conversion at their interface. The reflection coefficient of P-wave (R_P), reflected S-wave data (R_S), transmission coefficient of P-wave (T_P), and transmission coefficient of S-wave (T_P) are defined as follows:

$$\begin{cases} R_P = \frac{(\sin^2 \beta_2 / \sin^2 \alpha) \sin(2\alpha) - \cos(2\beta_2) \tan \varphi}{(\sin^2 \beta_2 / \sin^2 \alpha) \sin(2\alpha) \tan(2\beta_2) + \cos(2\beta_2)} \tan(2\beta_2) \\ R_S = \frac{(\sin^2 \beta_2 / \sin^2 \alpha) \sin(2\alpha) - \cos(2\beta_2) \tan \varphi}{(\sin^2 \beta_2 / \sin^2 \alpha) \sin(2\alpha) \tan(2\beta_2) + \cos(2\beta_2)} \\ T_P = \frac{\cos(2\beta_2) + \sin(2\beta_2) \tan \varphi}{(\sin^2 \beta_2 / \sin^2 \alpha) \sin(2\alpha) \tan(2\beta_2) + \cos(2\beta_2)} \\ T_S = \frac{(\sin^2 \beta_2 / \sin^2 \alpha) \sin(2\alpha) - \cos(2\beta_2) \tan \varphi}{(\sin^2 \beta_2 / \sin^2 \alpha) \sin(2\alpha) \tan(2\beta_2) + \cos(2\beta_2)} \end{cases} \tag{4}$$

Reflection and transmission coefficients determine the distribution of explosion energy at the rock-backfill interface. Specifically, the values of these coefficients accurately describe how the explosion energy is redistributed between the two media when the explosive stress wave propagates to the rock and backfill interface: a portion of the energy is reflected back into the rock medium, while another portion penetrates the interface into the backfill. This energy distribution ratio is crucial for evaluating blasting effectiveness, predicting the dynamic response of the surrounding rock and the backfill, and ensuring the safety of mining or underground engineering.

Experimental scheme

Digital image correlation synchronous measurement system

Principle of the digital image correlation method

Digital Image Correlation (DIC) is an optical, non-contact metrology technique that quantifies full-field displacement and strain by computationally correlating the grayscale intensity patterns of random speckles on a specimen's surface as it deforms[28].

In the initial stage of the experiment, a set of speckle images of the undeformed state is first acquired as a reference baseline; subsequently, based on the grayscale distribution characteristics of a reference sub-region, a target sub-region with high similarity is identified through a correlation matching algorithm; finally, by comparing the image grayscale information before and after deformation, the displacement field distribution is accurately calculated using the displacement changes of feature points within the sub-region. Figure 2 illustrates the underlying principle of this method. The detailed process is outlined below[29]:

A square region selected before deformation is taken as the reference sub-region, and its center point is denoted as M. After the specimen undergoes deformation, this reference sub-region experiences spatial displacement and geometric deformation, forming a corresponding target sub-region. According to the principle, the distance between the center points of the reference sub-region and the target sub-region can be expressed as:

$$\begin{cases} u = x'_0 - x_0 \\ v = y_0' - y_0 \end{cases} \tag{5}$$

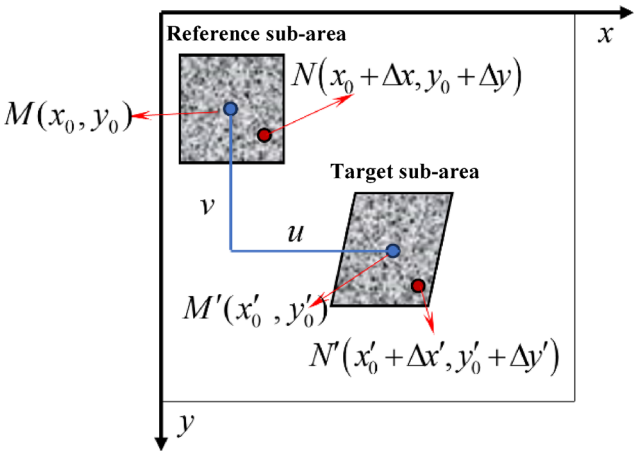

Fig. 2. The basic principles of the DIC method.

Another point *N* is selected within the reference sub-region. Let the horizontal and vertical coordinate distances between *M* and *N* be considered. After deformation, the sub-region undergoes not only translation but also rotation. Then, the relationship between *N* and its corresponding point *N'* is:

$$\begin{cases} x'_0 + \Delta x' = x_0 + u + \Delta x + \frac{\partial u}{\partial x}\Delta x + \frac{\partial u}{\partial y}\Delta y \\ y'_0 + \Delta y' = y_0 + v + \Delta y + \frac{\partial v}{\partial x}\Delta x + \frac{\partial v}{\partial y}\Delta y \end{cases} \tag{6}$$

Equation 6 describes the displacement relationship between two points under uniform deformation conditions. However, in practical applications, materials often exhibit non-uniform deformation characteristics. To improve the accuracy of coordinate calculation, second-order shape functions are introduced for coordinate transformation, which will not be elaborated here. In the displacement field calculation process, the correlation matching between the reference sub-region and the target sub-region is a key step for achieving accurate displacement calculation, and its matching accuracy directly determines the calculation accuracy of the final displacement field. The following is the expression for the correlation coefficient *F*, based on the principle of least squares:

$$F_1 = \sum_{m=-d}^{d}\sum_{n=-d}^{d}\left[f(x_m, y_n) - g(x_m{}', y_n{}')\right]^2 \tag{7}$$

In the equation, $f(x_m, y_n)$ represents the grayscale value of the reference sub-region, and $g(x'_m, y'_n)$ represents the grayscale value of the target sub-region. $(2d+1)$ is the side length of the square sub-region, where *d* is the pixel distance from the center of the sub-region to its edge.

Experimental setup

The Digital Image Correlation synchronous measurement system (Fig. 3) used in this study consists of three core modules: an illumination system, an image acquisition system, and a data storage and processing system. The illumination system includes a flash lamp controller and two xenon flash lamp units. Its flash duration is set to 2 ms, and the light intensity follows a normal distribution over time, providing a stable illumination environment and ideal optical contrast for the experiments. The image acquisition unit utilizes a high-performance high-speed camera. In this experiment, the camera's recording frame rate was 500,000 fps. The data storage and processing system comprises a computer workstation, camera control software, and image analysis software. The system achieves microsecond-level synchronization between the explosive detonation and high-speed image acquisition via a precision timing controller, ensuring the accurate acquisition of dynamic deformation data.

Specimen design

In this experiment, Polycarbonate (PC) was selected as the specimen material. This material exhibits isotropic characteristics and excellent ductility, enabling effective characterization of the propagation and evolution patterns of explosive stress waves. The dimensions of the specimens used in the experiment were 315 mm × 315 mm × 5 mm, and their dynamic mechanical parameters are detailed in Table 1.

A single-hole charge design was adopted. A cylindrical charge hole with a diameter of 5 mm was pre-fabricated at the center of the specimen. The charge quantity was 100 mg of RDX explosive. An inclined flaw measuring 160 mm × 5 mm was pre-fabricated at a distance of 60 mm from the center of the charge hole. The flaw was inclined at an angle of 45° to the horizontal direction, as shown in Fig. 4. Both the charge hole and the flaw were fabricated using a high-precision laser cutting process to ensure accuracy and consistency.

The filling materials used to create different wave impedance interfaces were clay, gypsum, and epoxy resin. Given the significant differences in the wave impedance of these three materials, this experiment allows for an

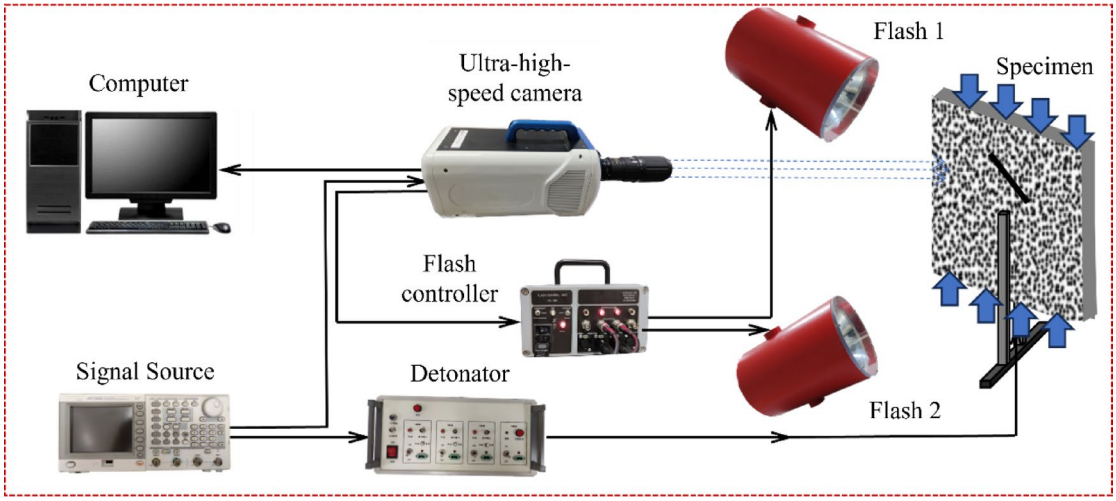

Fig. 3. Digital image correlation synchronous measurement system.

P-wave velocity/m s^{-1}	S-wave velocity/m s^{-1}	Elastic modulus/GPa	Poisson's ratio	Density/kg m^{-3}	Shear modulus/GPa
2125	1090	4.5	0.32	1449	1.7

Table 1. Mechanical parameters of PC material[30].

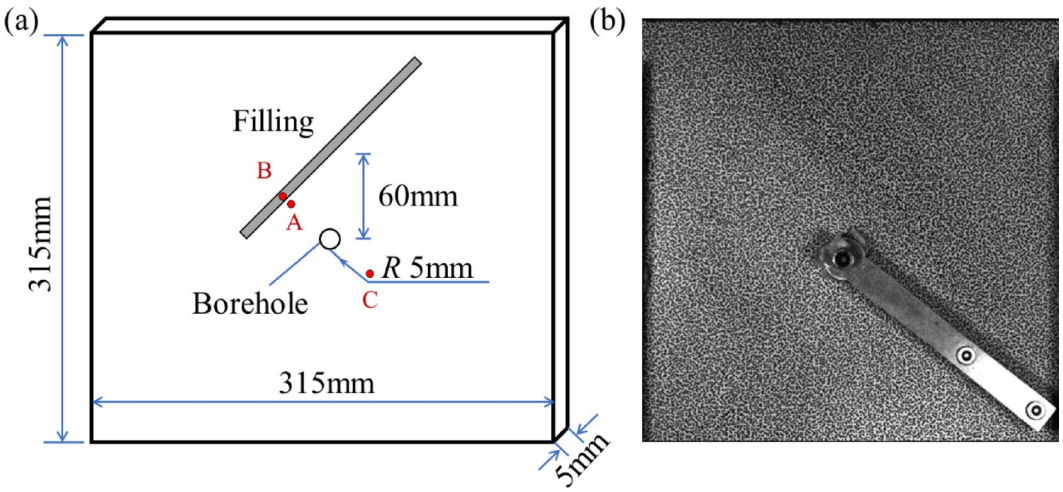

Fig. 4. (**a**) Schematic of PC model and (**b**) photograph of the specimen before the experiment.

in-depth investigation into the influence of different filling media on the wave propagation characteristics of explosive stress waves.

To prepare the specimen surface for Digital Image Correlation (DIC) analysis, a computer-assisted digital speckle pattern preparation technique was employed. This method first involves using computer software to randomly generate a digital speckle image according to preset quality parameters. The generated image is then high-precision printed onto the specimen surface. The final speckle pattern has a density of approximately 75% and an average speckle size of about 5 pixels, ensuring accurate displacement tracking and strain calculation during the dynamic event.

The preparation process for the three filling materials is as follows: For clay, an appropriate amount of dry clay powder was mixed with water to form a uniform paste, which was then filled and compacted. For gypsum, the gypsum powder was mixed with water according to a specific ratio and then poured. For epoxy resin, the main agent and the hardener were mixed according to the manufacturer's instructions and then injected. All filling materials were cured and dried inside the flaw for over 24 h to ensure a good bond with the PC plate.

Evolution of specimen strain field under explosion

Von mises strain evolution

After the explosion experiment, speckle images of the specimen surface were acquired using high-speed photography techniques. These images were then processed using Vic-2D software for data analysis to calculate and obtain the Von Mises full-field strain distribution of the specimen at different time instants after the explosion. Von Mises strain, based on the Von Mises yield criterion, comprehensively considers the maximum and minimum principal strains of the material under a three-dimensional stress state. It can comprehensively describe the overall deformation characteristics of the medium and, to a certain extent, reflect the propagation process of the explosive stress wave.

Figure 5 shows the full-field evolution process of Von Mises strain for specimens with different filling materials. The experiment primarily focuses on the strain changes in the early stage of the explosion (0 to 120 μs). Taking Fig. 5a as an example, the shock wave generated by the explosive detonation forms a high-strain zone near the borehole. As the shock wave gradually attenuates and transforms into a stress wave, the Von Mises strain propagates outwards in a circular pattern centered at the borehole, and its magnitude gradually decreases with increasing distance from the borehole center. Around $t = 20$ μs, the stress wave contacts the backfill, and its wave characteristics undergo significant changes. At the rock-backfill interface on the side closer to the borehole, reflection and transmission phenomena occur, respectively generating a reflected wave propagating towards the borehole and a transmitted wave entering the interior of the backfill. When the transmitted wave propagates within the backfill to the rock-backfill interface on the side farther from the borehole, it again undergoes reflection and transmission. During the period from $t = 40$ to $t = 90$ μs, as the stress wave continues to propagate along the rock-backfill interface, the aforementioned reflection and transmission processes are continuously repeated in the region between the borehole and the backfill, as well as inside the backfill, causing these areas to remain in a high-strain state. Meanwhile, at $t = 90$ μs, the stress wave encountering the backfill undergoes diffraction and superimposes with the transmitted wave that has penetrated the backfill, continuing to propagate outwards. However, its intensity is significantly reduced, indicating that the backfill has a significant blocking effect on the explosive stress wave. At $t = 120$ μs, the explosion process is substantially over. A high-strain zone still exists around the borehole, indicating that under the blasting load, the backfill and the area around the borehole underwent plastic deformation, resulting in significant residual strain. Other regions, after the stress wave has passed, return to their original state and belong to the elastic deformation zone.

The aforementioned results indicate that the existence of the rock-backfill interface has a significant influence on the propagation characteristics of explosive stress waves, and the influence of different filling materials on this process also cannot be ignored. When clay is used as the filling material, during the period from $t = 40$ μs to $t = 90$ μs, it can be clearly observed that significant reflection occurs when the stress wave is incident on the clay. This, in turn, leads to the generation of higher strain around the rock-backfill interface, and the blocking effect of the backfill on the explosive stress wave is quite pronounced at this time. This phenomenon is rooted in the significant mismatch between the wave impedances of the two materials. Specifically, as shown in Table 2, the wave impedance of PC material (3.08×10^6 kg (m^{-2} s^{-1})) is much greater than that of clay (1.87×10^6 kg (m^{-2} s^{-1})). According to wave theory, when a stress wave is incident from a high wave impedance medium to a low wave impedance medium, the reflected wave undergoes phase reversal. This large quantitative difference in wave impedance leads to a large absolute value of the reflection coefficient, and consequently, a stronger intensity of the reflected tensile wave. A smaller transmission coefficient means that a lower proportion of energy is transmitted into the low wave impedance medium, and the peak stress of the transmitted wave will be significantly reduced relative to the incident wave.

When gypsum is used as the filling material, the evolution process of the strain field is shown in Fig. 5b. At $t = 60$ μs, the strain field does not exhibit circular propagation but rather fluctuates around the backfill, and the strain near the rock-backfill interface is relatively high. At $t = 70$ μs, the strain on the outer side of the backfill is lower than on the side without the backfill. At $t = 120$ μs, when the explosion process is substantially over, higher residual strain still exists near the backfill, but it is lower than that observed with the clay filling material. Furthermore, the backfill also exhibits a blocking effect on the explosive stress wave. Evidently, when the backfill material is gypsum, the propagation process of the explosive stress wave also undergoes relatively significant reflection. Unlike the case with clay material, the wave impedance of gypsum (6.03×10^6 kg (m^{-2} s^{-1})) is significantly higher than that of the PC material (3.08×10^6 kg (m^{-2} s^{-1})), so the stress wave is incident from a low wave impedance medium (PC) to a high wave impedance medium (gypsum). Although this large wave impedance difference also leads to reflection phenomena, because the relative difference is slightly smaller than that of the PC-clay interface, the reflection intensity is also slightly lower, and the blocking effect of the backfill on the explosive stress wave is relatively weaker.

When epoxy resin is the filling material, the evolution of the strain field differs significantly from that of the previous two materials, as shown in Fig. 5c. During the period from $t = 40$ μs to $t = 90$ μs, no significant reflection phenomenon is observed, and the rock-backfill interface shows no distinct features. After the explosion ends at $t = 120$ μs, the strain value near the backfill is almost the same as that on the side without filling, and the backfill shows no obvious blocking effect on the explosive stress wave. This is because both PC material and epoxy resin are common engineering plastics with similar types of molecular structures, leading to their molecular packing densities and elastic moduli being relatively close. Consequently, their wave impedances are almost identical, with values of 3.08×10^6 kg (m^{-2} s^{-1}) for PC and 3.06×10^6 kg (m^{-2} s^{-1}) for epoxy resin. This near-perfect impedance matching means that the reflection coefficient at the interface approaches zero, while the transmission coefficient is close to 1, resulting in a minimal impeding effect of the interface on stress wave propagation. Energy can be more effectively transmitted from one material to another, and the energy loss at the interface is also minimized.

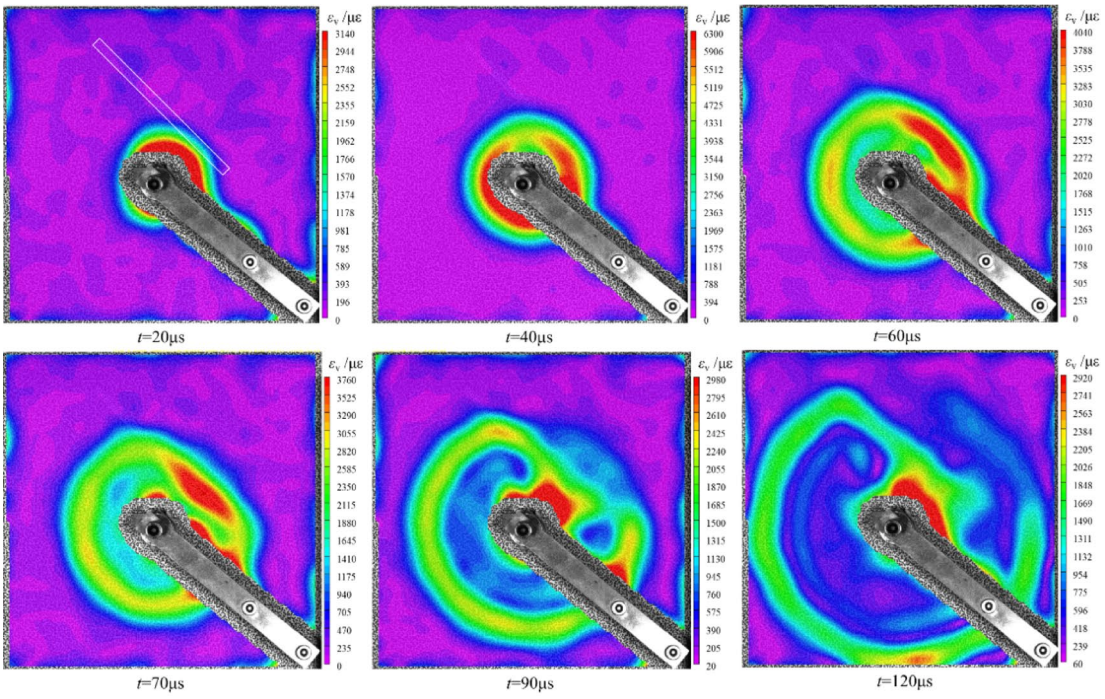

(a) Clay

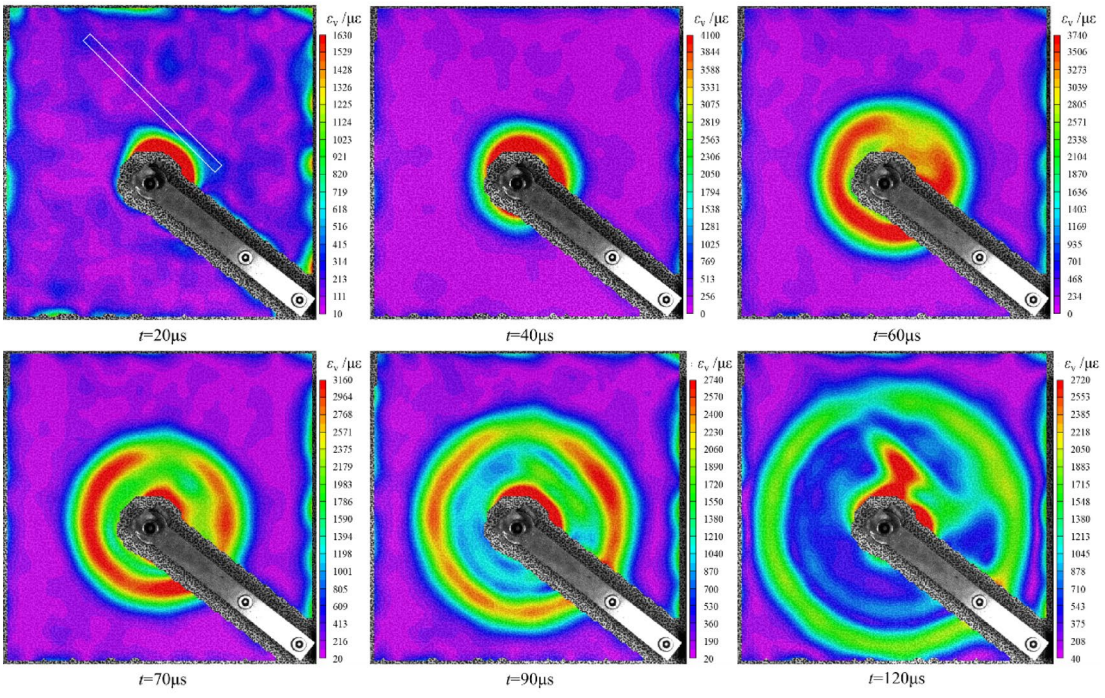

(b) Gypsum

Fig. 5. Evolution of effective strain field during the explosion process. (**a**) Clay, (**b**) gypsum, (**c**) epoxy.

To analyze the mechanical response of specimens with different filling materials, strain tests were conducted on specimens with three types of filling materials (epoxy resin, clay, and gypsum) at different measurement points (the locations of the measurement points are shown in Fig. 4a). The resulting strain time-history curves are shown in Fig. 6. The strain at measurement points A and C on the PC plate reached its peak value at approximately $t = 50$ μs. Among these, the peak strain of the epoxy resin specimen was significantly higher than that of the clay and gypsum specimens; however, its final strain value after the explosion was lower than that of the other two types of specimens. Observing the strain changes at different measurement points on the

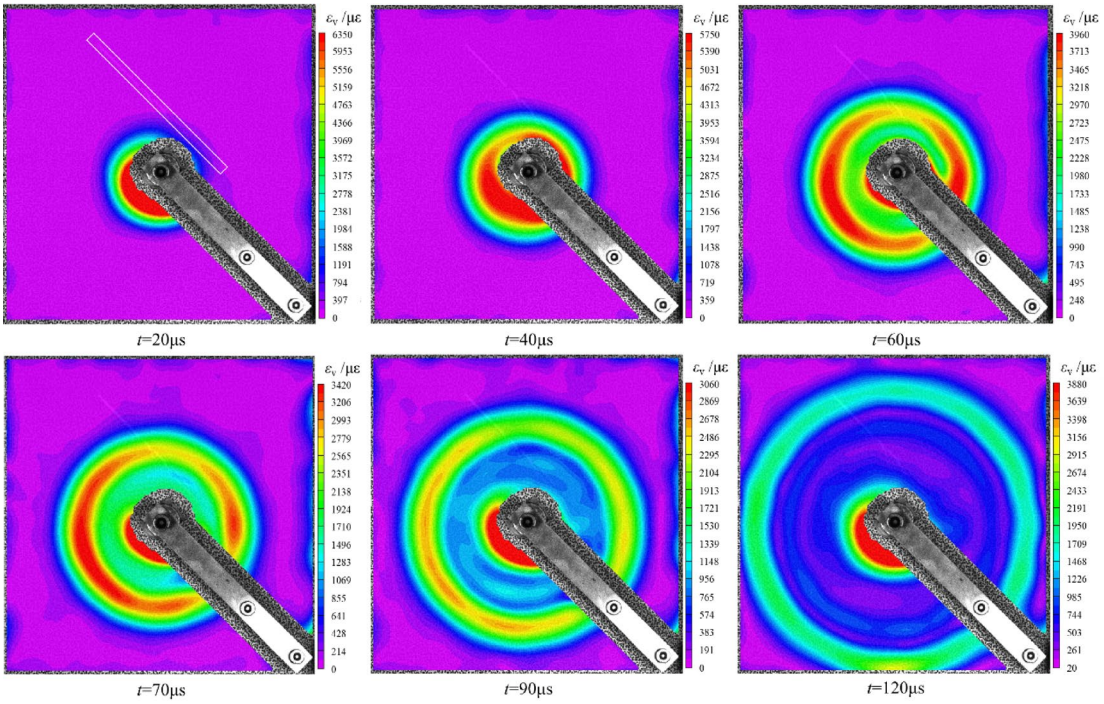

(c) Epoxy

Fig. 5. (continued)

Filling material	Density/kg m^{-3}	*P*-wave velocity/m s^{-1}	Wave impedance/kg (m^{-2} s^{-1})
PC	1449	2125	3.08×10^6
Clay[31]	1700	1100	1.87×10^6
Gypsum[32]	2320	2600	6.03×10^6
Epoxy resin[33]	1200	2550	3.06×10^6

Table 2. Physical and mechanical properties of filling materials.

same type of specimen, the strain values at points A and B for the clay and gypsum specimens were significantly higher than at point C. In contrast, for the epoxy resin specimen, the difference in strain values among its various measurement points was not significant. This phenomenon can be attributed to differences in material wave impedance: the wave impedance of epoxy resin is close to that of the PC specimen material, leading to weaker reflection of the explosive stress wave and less energy dissipation. This results in higher peak strain at the measurement points, but the final degree of damage to both the specimen and the backfill is relatively uniform. Conversely, for the clay and gypsum specimens, the wave impedance difference (with PC) is larger, causing the explosive stress wave to produce stronger reflections during propagation, and part of the energy is dissipated, leading to lower peak strain. However, due to continuous incidence, reflection, and transmission occurring at the interface, the final strain value is instead higher for these materials (clay and gypsum).

Horizontal strain analysis

Since effective strain, as a scalar quantity, only reflects the degree of material deformation and cannot distinguish between tensile and compressive stress states, it cannot directly provide directional information about the stress state when analyzing the explosive mechanical behavior of the specimen. For this reason, we need to examine strain components in specific directions, such as horizontal strain. By observing its positive and negative values (where a positive value indicates tension and a negative value indicates compression), we can accurately monitor and analyze the changes in the tensile and compressive states of the material during the loading process.

Taking the clay-filled specimen as an example, the evolution process of the horizontal strain field under a Cartesian coordinate system is analyzed, as shown in Fig. 7. In the figure, blue-purple regions represent compressive strain zones, while red-yellow regions represent tensile strain zones. For horizontal strain, at $t = 20$ μs, under the action of the explosive stress wave, "fan-shaped" compressive strain zones appear on the left and right sides of the borehole. Due to the dynamic Poisson's ratio effect, tensile strain zones appear on the upper and lower sides of the borehole. As the explosive stress wave propagates, the compressive zones on the left and

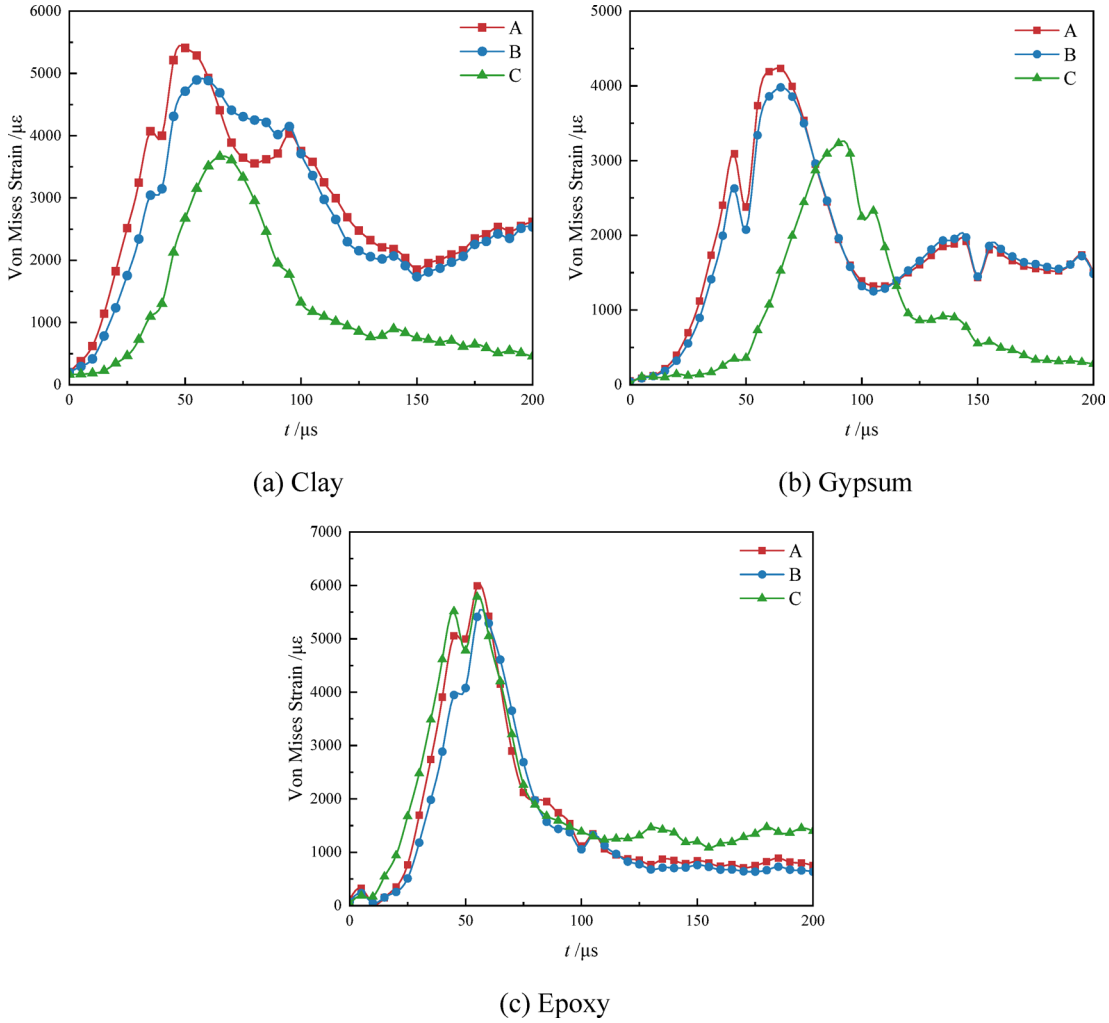

Fig. 6. Strain time-history curves at relevant measurement points. (**a**) Clay, (**b**) gypsum, (**c**) epoxy.

right sides expand outwards in a "crescent" shape, and a thinner tensile strain zone forms behind them. This is due to the gradual release of elastic energy from the compressed deformation zone, which in turn forms the tensile zone; this is also the main reason why the tensile zone closely follows the compressed zone. Additionally, the tensile strain zone on the upper side of the borehole extends towards the location of the backfill. The backfill obstructs the propagation of this tensile strain zone, and reflection and diffraction occur at the backfill interface. Due to reflection at the backfill interface, a convergence of the tensile strain zone is caused on the lower side of the backfill, which also leads to the formation of a compressive strain zone there. Throughout the entire propagation process, the compressive and tensile strain zones undergo significant attenuation. As for the vertical strain evolution, since the evolution process of its strain field is similar to that of the horizontal strain field, it will not be elaborated here.

Numerical methodology

Overview of the numerical model

Full-field strain evolution contour maps of the PMMA medium under blasting load were obtained using Digital Image Correlation (DIC) technology, visually demonstrating the strain distribution and evolution trends on the material surface. Although PMMA is widely used as a rock-like material due to its mechanical properties being similar to those of rock, the inherent differences in their properties mean that the validity of directly extrapolating PMMA-based experimental results to real rock still requires assessment. Furthermore, the inherent limitations of experimental measurements also restrict a complete analysis of processes occurring at the microsecond level, such as stress wave propagation, interface reflection and transmission, and wave system superposition. Therefore, to compensate for the deficiencies of experimental observations and to specifically analyze the full-field wave propagation process of explosive stress waves and crack propagation behavior in real rock media, this study further utilizes numerical simulations to validate experimental phenomena and deepen the understanding of stress wave propagation mechanisms.

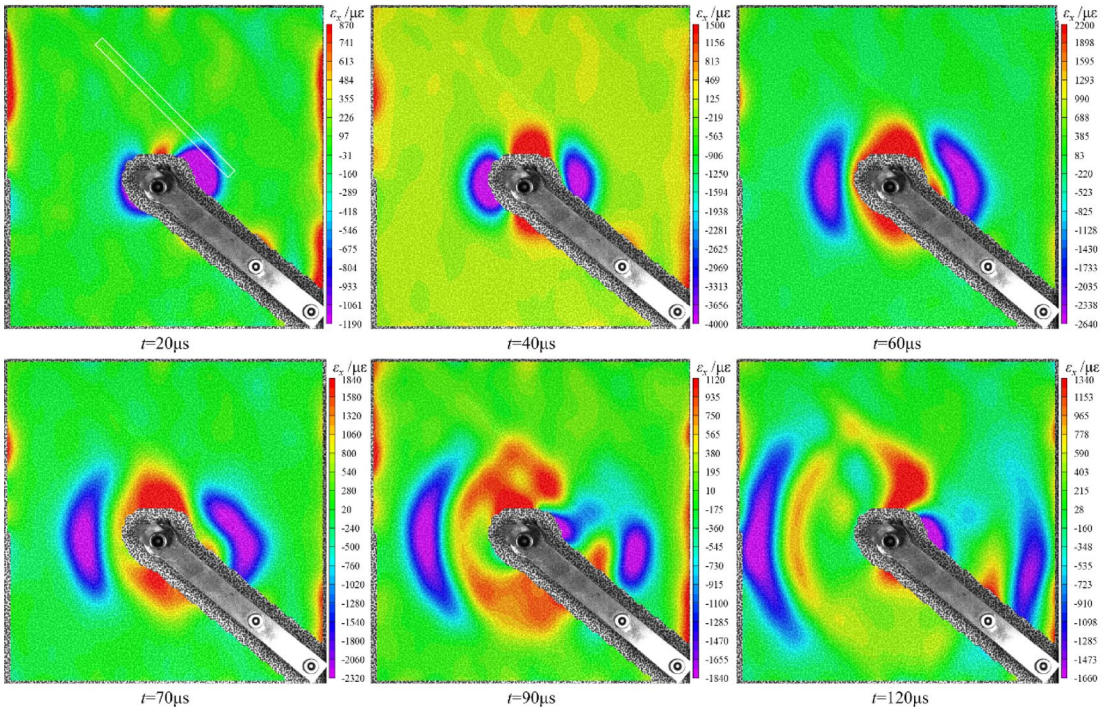

Fig. 7. Evolution of horizontal strain field during the blasting process.

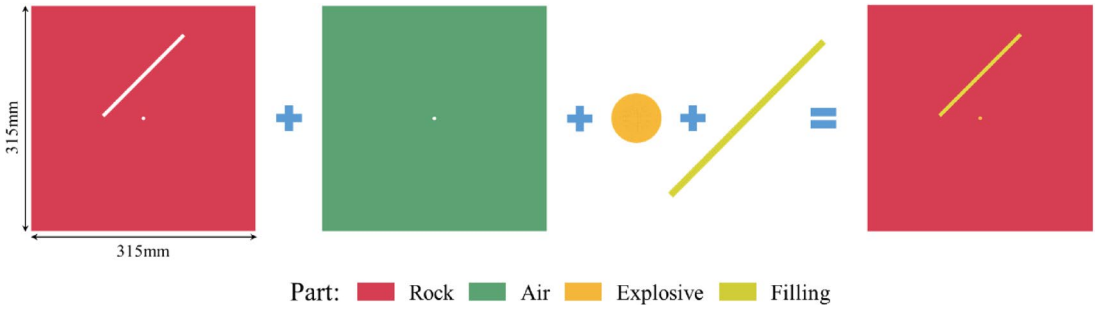

Fig. 8. Schematic diagram of the numerical model.

Model establishment

This study employs LS-DYNA software to establish a 2D numerical model, with dimensions identical to the physical experimental specimens (315 mm × 315 mm). Considering that blasting is a typical fluid-structure interaction (FSI) dynamic problem, the model consists of four parts: rock, backfill, explosive, and air, as shown in Fig. 8, and is solved using a multi-algorithm coupling approach.

The rock and backfill, as the solid parts, are described using the Lagrangian algorithm and discretized with solid elements. The explosive and air, as the fluid parts, are modeled using the multi-material Arbitrary Lagrangian-Eulerian (ALE) algorithm, as they undergo extreme large deformations during the explosion. The interaction between the fluids and solids is implemented using the *CONSTRAINED_LAGRANGE_IN_SOLID keyword, which efficiently and stably handles the transmission of the blasting load.

The contact interface between the rock and the backfill is simulated using the *CONTACT_AUTOMATIC_SURFACE_TO_SURFACE_TIEBREAK algorithm. This is a stress-failure-based tiebreak contact that can realistically simulate the transmission and reflection of stress waves at the interface, as well as potential debonding failure. To eliminate the interference of boundary-reflected waves on the calculation results, non-reflecting boundary conditions are applied to all external boundaries of the model to simulate an infinite domain environment.

The finite element mesh of the model is shown in Fig. 9. To accurately capture the stress gradients and crack initiation in the near-borehole zone, the mesh around this area is refined. The entire model consists of 181,423 elements.

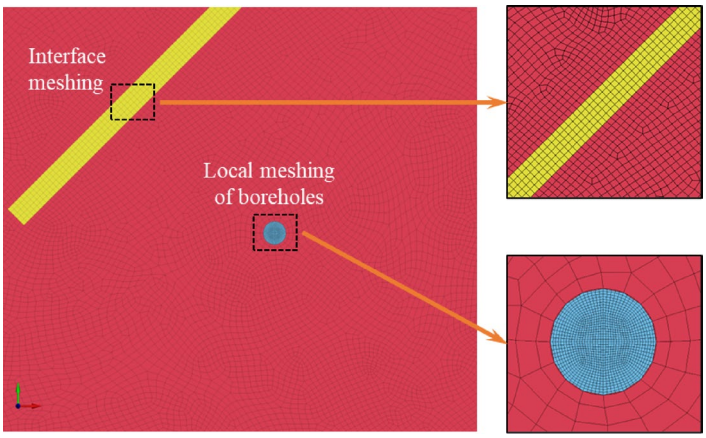

Fig. 9. Model meshing details.

ρ/kg m^{-3}	G_1/MPa	f_c/MPa	f_t^*	f_s^*	g_c^*	g_t^*
*MAT_RHT						
2265	5578.5	24	0.0894	0.18	0.53	0.7
B	A	N	β_c	β_t	D_1	D_2
0.0105	1.6	0.61	0.043	0.045	0.04	1.0

Table 3. Rock material parameters.

ρ/kg m^{-3}	Detonation velocity/m s^{-1}	Detonation pressure/GPa	Initial specific energy/J m^{-3}
931	4160	5.15	3.87×10^9

Table 4. Explosive material and JWL equation of state parameters.

Material parameters

The RHT (Riedel-Hiermaier-Thoma) model was selected for the rock material. This model incorporates characteristics such as strain rate effect, strain hardening, and damage softening. Therein, the expression for failure stress as a function of hydrostatic pressure p, Lode angle θ, and strain rate is:

$$\sigma_{eq}^*(p,\theta,\dot{\varepsilon}) = Y_C(p)R_3(\theta)F_{\text{rate}}(\dot{\varepsilon}) \tag{8}$$

$$Y_C(p) = A\left(p^* - p_{\text{spall}}^* F_{\text{rate}}(\dot{\varepsilon})\right)^N \tag{9}$$

In the equation: $R_3(\theta)$ is an angular function on the deviatoric plane (Lode angle dependence function); $F_{\text{rate}}(\dot{\varepsilon})$ is the strain rate enhancement factor; $Y_C(p)$ is the equivalent stress on the compressive meridian. A and N are failure surface parameters; p^* is the normalized hydrostatic pressure; p_{spall}^* is the normalized spall strength. The RHT model parameters are detailed in Table 3.

For the explosive, the *MAT_HIGH_EXPLOSIVE_BURN model was selected, and the Jones-Wilkens-Lee (JWL) equation of state (EOS) is used to describe the relationship between volume, pressure, and energy of the detonation products. The determined detonation pressure is:

$$p_e = A_e\left(1-\frac{\omega}{R_1V}\right)e^{-R_1V} + B_e\left(1-\frac{\omega}{R_2V}\right)e^{-R_2V} + \frac{\omega E_0^e}{V} \tag{10}$$

In the equation: p_e is the detonation pressure determined by the JWL equation of state; A_e, B_e, R_1, R_2, and ω are explosive material constants; E_0^a is the initial internal energy per unit volume of the explosive; V is the initial relative volume. Specific parameters for the explosive material and the JWL equation of state are detailed in Table 4. Wherein, v_d and P_{cj} represent the detonation velocity and Chapman-Jouguet (CJ) pressure of the explosive, respectively.

For the air material, the typical *MAT_NULL material model is used, in conjunction with the *EOS_LINEAR_POLYNOMIAL linear polynomial equation of state to define the relationship between gas pressure, density, and internal energy. Specific parameters for air are detailed in Table 5.

$\rho/(kg\ m^{-3})$	C_0	C_1	C_2	C_3	C_4	C_5	C_6	$E_0^{\alpha}/(kj\ m^{-3})$
1.2	0	0	0	0	0.4	0.4	0	250

Table 5. Air material and EOS (Equation of State) parameters.

Serial number	Density/kg m^{-3}	Velocity of wave/m s^{-1}	Wave impedance/kg (m^{-2} s^{-1})
A-1	2265	3031.1	6.87×10^6
B-1	2540	3151.7	8.01×10^6
B-2	2300	4775.7	10.98×10^6
B-3	2416	6031.1	14.57×10^6

Table 6. Wave impedance of different filling materials.

For the backfill material selection, three types of backfill materials with different wave impedances were established to create varying impedance gradients, and the HJC (Holmquist-Johnson-Cook) model was used for their characterization. Specific parameters are detailed in Table 6. Therein, A-1 denotes the rock material parameters, while B-1, B-2, and B-3 denote the parameters for the three different filling media. The interface contact between the rock and the backfill is handled by setting the contact keyword *CONTACT_AUTOMATIC_SURFACE_TO_SURFACE_TIEBREAK. This method accurately handles stress wave transmission and reflection at the interface, and allows for the assessment of stability and effectiveness between the backfill and the surrounding rock.

Analysis of simulation results

Wave propagation characteristics of explosive stress waves

Figure 10 reveals the spatio-temporal evolution patterns of effective stress in different specimens under explosive loading. Taking the specimen shown in Fig. 10a as an example, the results indicate that after explosive detonation, the generated explosive stress wave propagates outwards with an approximately circular wavefront, and its amplitude attenuates with increasing propagation distance. At $t = 14$ μs, the stress wavefront reaches and acts upon the front interface of the backfill, subsequently exciting a transmitted stress wave within the backfill, causing the backfill region to transform into a high-stress state. Simultaneously, a reflected wave is generated at the lower contact interface between the backfill and the surrounding rock; this reflected wave propagates towards the borehole. By $t = 16$ μs, the transmitted wave has propagated to the upper interface of the backfill, where transmission and reflection phenomena occur again, leading to further expansion of the high-stress region within the backfill. At $t = 18$ μs, part of the stress wave energy continues to penetrate the backfill, while diffraction occurs at the lower edge of the backfill, with the diffracted wave continuing to propagate along the side of the backfill. Subsequently, at $t = 26$ μs, the diffracted wave that has passed around the end of the backfill meets and superimposes with the transmitted wave that has penetrated the backfill, and they continue to propagate outwards. By $t = 42$ μs, the stress wave also undergoes diffraction at the upper edge of the backfill. This series of stress wave evolution processes is broadly similar to the experimental observation results.

Integrating the experimental results from Fig. 5 with the stress wave propagation characteristics presented in the Fig. 10 simulations, it is clear that the presence of the backfill significantly influences the propagation path and energy distribution of the explosive stress wave. Its main effects are manifested as follows: Firstly, the backfill constitutes a significant obstacle to stress wave propagation, evidenced by distinct reflected waves; Secondly, after the stress wave bypasses or passes through the backfill via transmission and diffraction, it propagates outwards, and wave superposition occurs in the region behind the backfill, disturbing the stress state in this area.

Crack propagation behavior

Due to the limitations of Digital Image Correlation (DIC) technology in analyzing the distribution characteristics of blast-induced cracks, this section employs numerical simulation methods to conduct an in-depth investigation into the damage characteristics of rock under conditions of different filling media.

As shown in Fig. 11, the figure presents damage contour maps of the rock and grayscale representation images of cracks extracted from these maps. The crack distribution characteristics show that in the regions at the top and bottom ends of the backfill, cracks exhibit significant guided propagation. Compared to the outer side of the backfill, the cracks on its inner side are more developed and dense. This phenomenon clearly reveals that the backfill has significant guiding effects and blocking effects on the propagation path of blast-induced cracks. The underlying physical mechanism is that when blast-induced cracks propagate to the rock-backfill interface, transmission and reflection of stress waves occur at the interface due to the difference in wave impedance between the two materials. Reflected waves cause energy concentration in the rock mass on the inner side of the backfill, leading to local accumulation of cracks in this region and subsequently inducing severe damage. Meanwhile, the stress concentration phenomenon at the top and bottom ends of the backfill, caused by geometric discontinuity and differences in material properties, induces cracks to preferentially propagate outwards along these ends.

Further observation shows that as the wave impedance difference between the rock and the backfill increases, the number of cracks on the outer side of the backfill gradually decreases. Taking the B-3 specimen as an example,

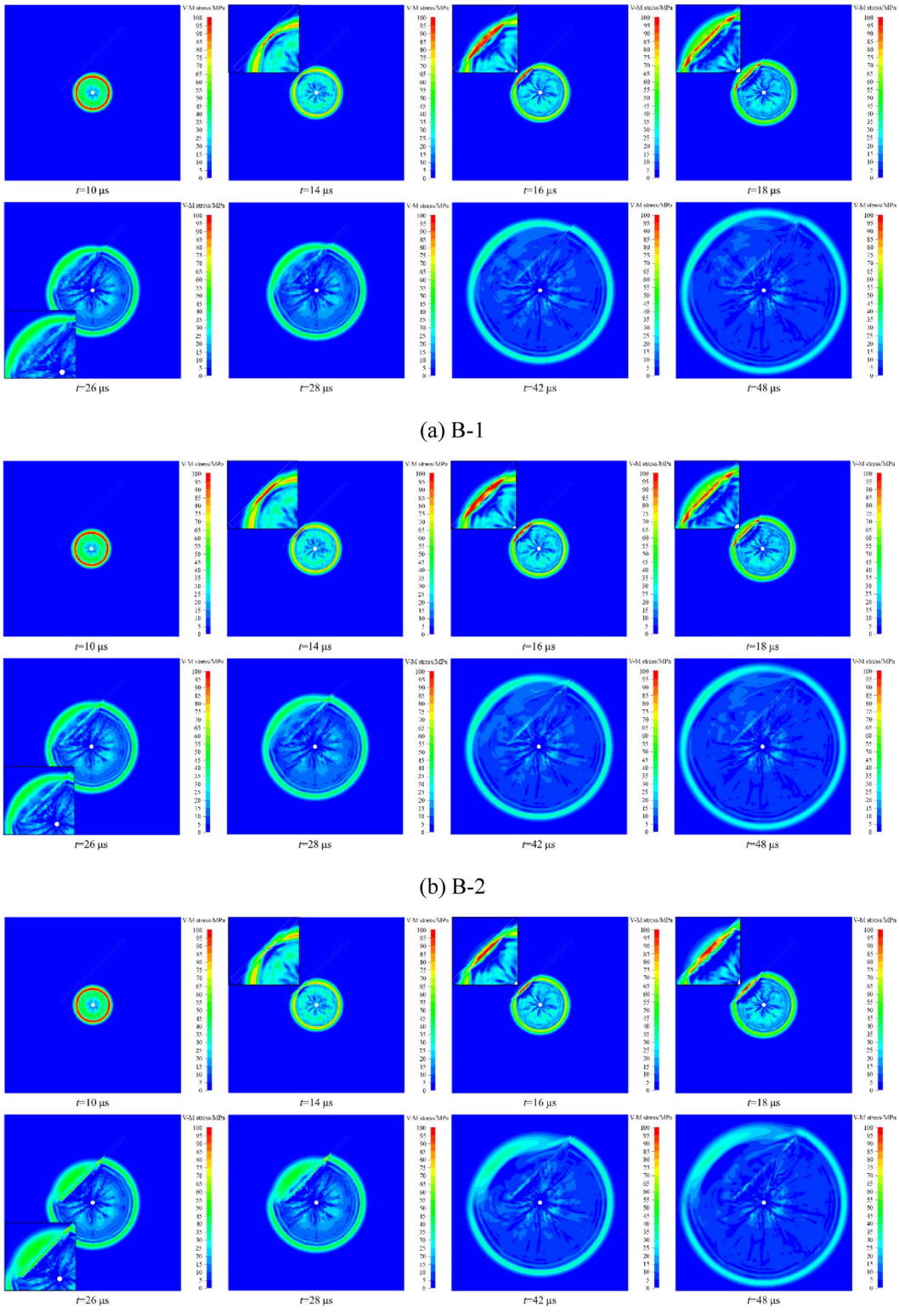

Fig. 10. Propagation process of explosive stress wave. (**a**) B-1, (**b**) B-2, (**c**) B-3.

almost no macroscopic cracks are observed on its outer side. In contrast, the extent of the damaged zone on the inner side of the backfill tends to expand and gradually extends along the backfill interface. This clearly indicates that the higher the wave impedance difference between the rock and the backfill, the more explosion energy is reflected back into the rock mass, thus causing its inner region to suffer more severe damage.

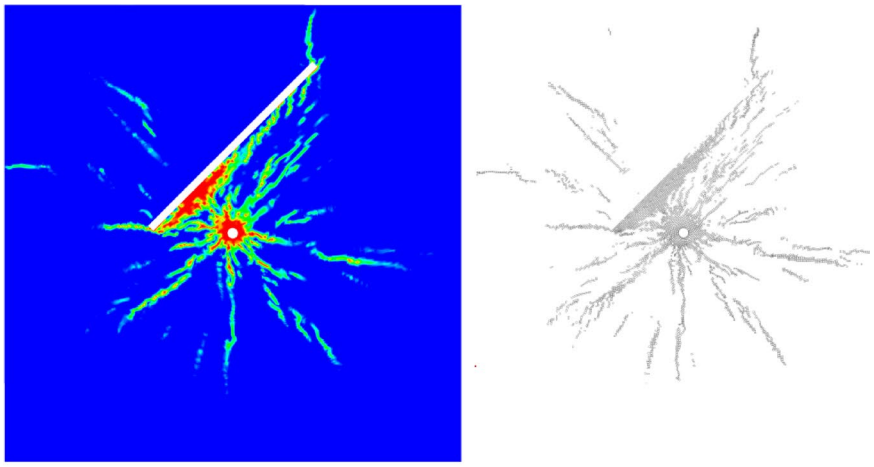

(a) B-1

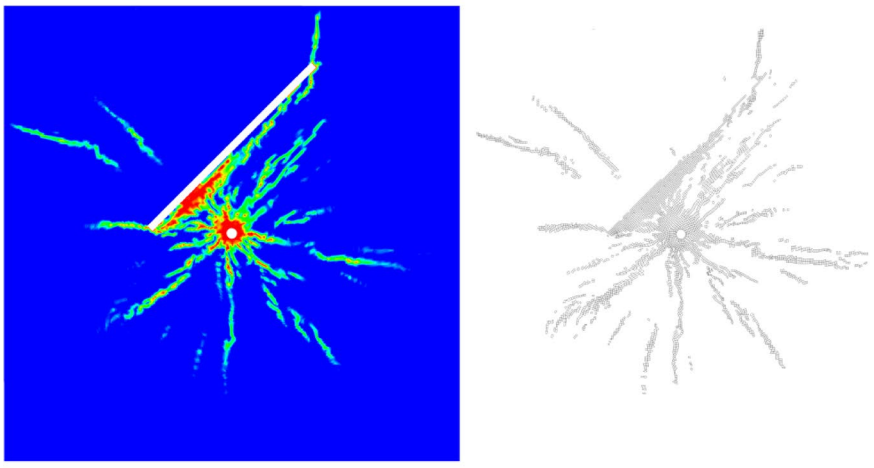

(b) B-2

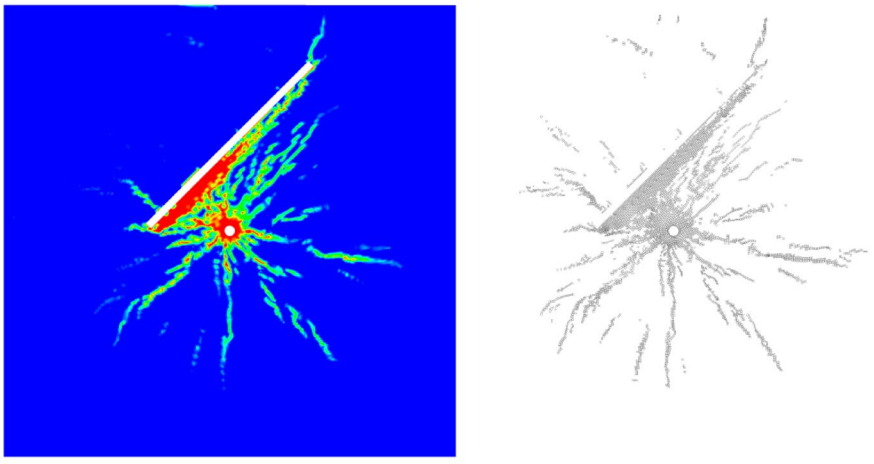

(c) B-3

Fig. 11. Post-blast crack distribution in the mode. (**a**) B-1, (**b**) B-2, (**c**) B-3.

To quantitatively analyze the post-blast crack distribution characteristics, rock fractal theory is introduced, and the fractal dimension of blast-induced cracks is calculated. Among these methods, the box-counting dimension method is a widely used technique for calculating fractal dimension. Its calculation formula is shown in Eq. (11):

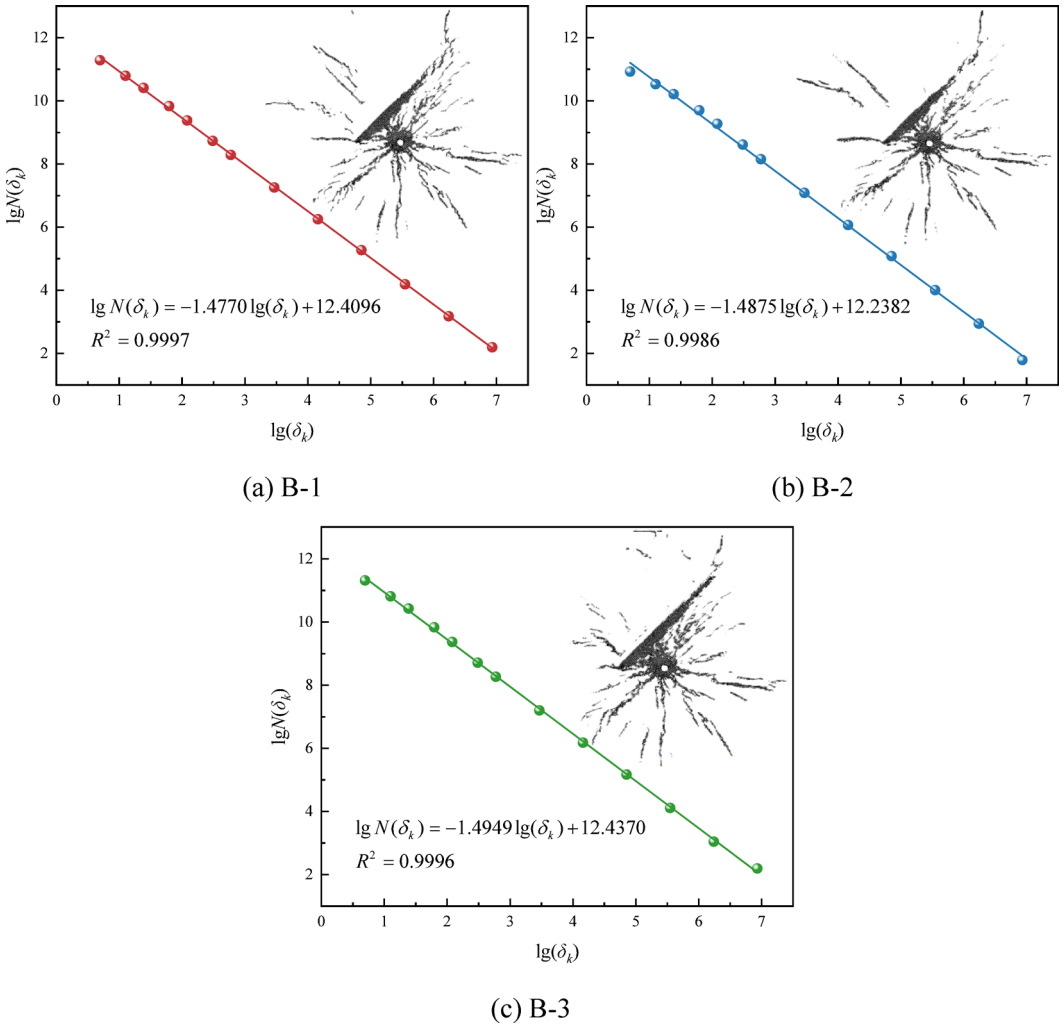

Fig. 12. Fractal dimension of blast-induced cracks. (**a**) B-1, (**b**) B-2, (**c**) B-3.

$$D_{\mathrm{b}} = \lim_{\delta_k \to \infty} \frac{\lg\ N\left(\delta_k\right)}{-\lg\ \delta_k} \tag{11}$$

In the equation, D_{b} is the fractal dimension; δ_k refers to the side length of the small squares used to cover the measured image; and $N(\delta_k)$ denotes the number of such small squares required to cover the image.

Figure 12 presents the calculation results of the fractal dimension for blast-induced cracks in different specimens. The fractal dimensions corresponding to the various specimens are 1.4770, 1.4875, and 1.4949, respectively. It is evident that the fractal dimension exhibits a monotonically increasing trend with the increase in wave impedance difference between the rock mass and the backfill. Combined with the preceding analysis of crack distribution characteristics, the backfill plays a significant blocking role in the propagation of blast-induced cracks, effectively suppressing the tendency of cracks to propagate along their original paths across the backfill interface. However, this blocking effect simultaneously promotes the accumulation, bifurcation, and coalescence of cracks in the region on the inner side of the backfill, leading to the formation of localized high-damage zones. This accumulation of cracks directly leads to an increase in the fractal dimension. The greater the wave impedance difference between the rock mass and the backfill, the more pronounced the aforementioned crack blocking effect and the induced secondary cracking effect become. This constitutes the primary mechanism for the increase in fractal dimension with the growing wave impedance difference.

Conclusions

This study comprehensively utilized the Digital Image Correlation (DIC) method and LS-DYNA numerical simulations to conduct an in-depth investigation into the influence mechanisms of different types of filling media and their wave impedance differences with rock on the propagation characteristics of explosive stress waves, rock mass strain response, damage patterns, and crack propagation behavior. The main conclusions are as follows:

1. The wave impedance difference between the filling medium and the rock is the core factor influencing the propagation of explosive stress waves and energy distribution. When this difference is large, the reflection effect at the backfill interface is significant, forming a "blocking effect," and more energy is reflected back into the rock mass. Conversely, when their wave impedances are similar, stress wave transmission is more effective, and the "blocking effect" is weaker.
2. The type of filling medium, by modulating the reflection and transmission of waves at the interface, determines the strain response and damage patterns of the rock mass. Filling with similar wave impedance leads to high peak strain at various points but relatively uniform final failure. Conversely, filling with a large wave impedance difference, despite potentially lower initial peak strain, results in greater final strain and plastic deformation due to the continuous action of the interface. Numerical simulations show that the greater the wave impedance difference, the more pronounced the "guiding" and "blocking" effects of the backfill on cracks, leading to intensified damage and crack accumulation on its inner side, which also results in a higher fractal dimension of the cracks.
3. In backfill mining practice, the wave impedance difference between the rock and the backfill has important guiding significance for surrounding rock stability and mining effectiveness. This suggests that when selecting backfill materials or designing blasting parameters, their wave impedance compatibility with the surrounding rock must be fully considered. To protect the stability of already backfilled areas or to reduce damage to the surrounding rock in subsequent mining zones, backfill materials with wave impedance close to that of the surrounding rock should be selected to minimize energy reflection and stress concentration. Conversely, if blasting energy is to be utilized to promote fragmentation of the rock mass in specific areas, exploiting wave impedance differences to guide and enhance crack propagation can be considered. Therefore, optimizing the wave impedance relationship between the backfill and the surrounding rock is key to controlling the extent of blasting damage, ensuring stope safety, and improving mining efficiency.

Finally, this study also recognizes that the macroscopic continuum model used in the numerical simulation did not consider the microstructural features of the rock, such as its mineralogical composition and grain structure, which are important factors influencing the crack propagation path and pattern. Future research will be dedicated to employing multi-scale numerical methods that can couple macroscopic and microscopic structures, with the aim of more accurately predicting and evaluating the blasting damage effects under real geological conditions.

Data availability

The datasets generated and/or analysed during the current study are not publicly available due [the nature of this research, participants did not consent for their data to be shared publicly] but are available from the corresponding author on reasonable request.

Received: 24 June 2025; Accepted: 8 September 2025
Published online: 09 October 2025

References

1. Huang, C. et al. Effect of prestress on propagation of blasting-induced main crack in specimens with empty hole. *Theoret. Appl. Fract. Mech.* **126**, 103928 (2023).
2. Yin, T. et al. Water saturation effects on the mechanical characteristics and fracture evolution of sandstone containing pre-existing flaws. *Theoret. Appl. Fract. Mech.* **122**, 103605 (2022).
3. Huang, C. et al. The effect of preloaded compressive stress and curvature of defect on blast-induced fracture behavior by caustic and numerical models. *Mathematics* **11**(21), 4532 (2023).
4. Wu, Y. K. et al. Propagation characteristics of blast-induced shock waves in a jointed rock mass. *Soil Dyn. Earthq. Eng.* **17**(6), 407–412 (1998).
5. Liu, Y. et al. Experimental investigation of the influence of joint geometric configurations on the mechanical properties of intermittent jointed rock models under cyclic uniaxial compression. *Rock Mech. Rock Eng.* **50**, 1453–1471 (2017).
6. Zhu, Q. et al. Mechanical properties and fracture evolution of sandstone specimens containing different inclusions under uniaxial compression. *Int. J. Rock Mech. Min. Sci.* **115**, 33–47 (2019).
7. Liang, X. et al. Visualization study on stress evolution and crack propagation of jointed rock mass under blasting load. *Eng. Fract. Mech.* **296**, 109833 (2024).
8. Ma, G. W., Fan, L. F. & Li, J. C. Evaluation of equivalent medium methods for stress wave propagation in jointed rock mass. *Int. J. Numer. Anal. Meth. Geomech.* **37**(7), 701–715 (2013).
9. Zhao, J. & Cai, J. G. Transmission of elastic P-waves across single fractures with a nonlinear normal deformational behavior. *Rock Mech. Rock Eng.* **34**, 3–22 (2001).
10. Li, J. C. et al. Analytical study for stress wave interaction with rock joints having unequally close–open behavior. *Rock Mech. Rock Eng.* **49**, 3155–3164 (2016).
11. Li, J. C. et al. A time-domain recursive method to analyse transient wave propagation across rock joints. *Geophys. J. Int.* **188**(2), 631–644 (2012).
12. Dong, Q., Li, X. P. & Liu, T. T. Influence of in-situ stress on the energy transmission of blasting stress wave in jointed rock mass. *Shock. Vib.* **2021**(1), 6822317 (2021).
13. Dong, Q., Li, X. P. & Huang, J. H. Model test study on cylindrical blasting stress wave propagation across jointed rock mass with different initial stresses. *Adv. Civ. Eng.* **2020**(1), 8881302 (2020).
14. Chen, X. et al. Experimental study on wave propagation across a rock joint with rough surface. *Rock Mech. Rock Eng.* **48**, 2225–2234 (2015).
15. Han, Z. et al. Experimental study of stress wave propagation and energy characteristics across rock specimens containing cemented mortar joint with various thicknesses. *Int. J. Rock Mech. Min. Sci.* **131**, 104352 (2020).
16. Jia, S. et al. Experimental and theoretical study on the propagation characteristics of stress wave in filled jointed rock mass. *PLoS ONE* **16**(9), e0253392 (2021).
17. Huang, X. et al. Stress wave propagation through rock joints filled with viscoelastic medium considering different water contents. *Appl. Sci.* **10**(14), 4797 (2020).

18. Wang, X. et al. Study on the influence of the joint angle between blast holes on explosion crack propagation and stress variation. *Processes* **11**(9), 2805 (2023).
19. Zhang, F. et al. Explosive stress wave propagation and fracture characteristics of rock-like materials with weak filling defects. *Eng. Fract. Mech.* **308**, 110372 (2024).
20. Zhao, F. et al. A review of fracture mechanic behaviors of rocks containing various defects. *Undergr. Space* **12**, 102–115 (2023).
21. Wong, R. H. C. et al. Analysis of crack coalescence in rock-like materials containing three flaws—part I: Experimental approach. *Int. J. Rock Mech. Min. Sci.* **38**(7), 909–924 (2001).
22. Tang, C. A. et al. Analysis of crack coalescence in rock-like materials containing three flaws—Part II: Numerical approach. *Int. J. Rock Mech. Min. Sci.* **38**(7), 925–939 (2001).
23. Wong, R. H. C. et al. Splitting failure in brittle rocks containing pre-existing flaws under uniaxial compression. *Eng. Fract. Mech.* **69**(17), 1853–1871 (2002).
24. Lee, H. & Jeon, S. An experimental and numerical study of fracture coalescence in pre-cracked specimens under uniaxial compression. *Int. J. Solids Struct.* **48**(6), 979–999 (2011).
25. Li, X. et al. Numerical study on the behavior of blasting in deep rock masses. *Tunn. Undergr. Space Technol.* **113**, 103968 (2021).
26. Zhu, J. et al. Stress wave propagation across jointed rock mass under dynamic extension and its effect on dynamic response and supporting of underground opening. *Tunn. Undergr. Space Technol.* **108**, 103648 (2021).
27. Yu, Q. et al. Numerical simulation of stress wave propagation in joint rock specimens with cavity defects. *Front. Earth Sci.* **10**, 971172 (2022).
28. Chu, T. C., Ranson, W. F. & Sutton, M. A. Applications of digital-image-correlation techniques to experimental mechanics. *Exp. Mech.* **25**, 232–244 (1985).
29. Sutton, M. A., Orteu, J. J. & Schreier, H. *Image Correlation for Shape, Motion and Deformation Measurements* (Springer, 2009).
30. Ding, C., Yang, R. & Feng, C. Stress wave superposition effect and crack initiation mechanism between two adjacent boreholes. *Int. J. Rock Mech. Min. Sci.* **138**, 104622 (2021).
31. Schön, J. H. *Physical Properties of Rocks: Fundamentals and Principles of Petrophysics* (Elsevier, USA, 2015).
32. Mavko, G., Mukerji, T. & Dvorkin, J. *The Rock Physics Handbook* (Cambridge University Press, 2020).
33. O'Donnell, M., Busse, L. J. & Miller, J. G. 1. Piezoelectric transducers. In *Methods in Experimental Physics* Vol. 19 29–65 (Academic Press, 1981).

Author contributions

H.W. conceived the study, designed the methodology, secured funding, and wrote the original manuscript draft. C.L. conducted the physical experiments and numerical simulations, curated the data, and prepared the figures. X.Z. performed the formal data analysis and validated the results. H.Q. provided resources and contributed to the conceptualization. All authors reviewed and edited the final manuscript.

Funding

This research was supported by: (1) China National Coal Group Corporation Major Science and Technology Special Funding Project (ZMYXM JT-22-02).

Declarations

Competing interests

The authors declare no competing interests.

Additional information

Correspondence and requests for materials should be addressed to H.W.

Reprints and permissions information is available at www.nature.com/reprints.

Publisher's note Springer Nature remains neutral with regard to jurisdictional claims in published maps and institutional affiliations.